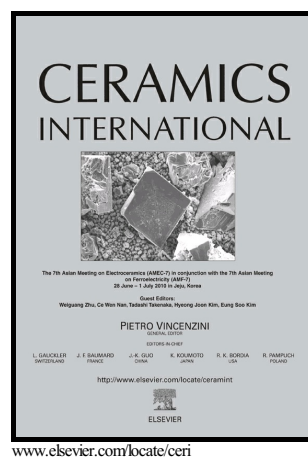


Phase-controlled SnO<sub>2</sub> and SnO Growth by Atomic Layer Deposition using Bis(*N*-ethoxy-2,2-dimethyl propanamido)tin Precursor

Hyo Yeon Kim, Ji Hyeun Nam, Sheby Mary George, Jin-Seong Park, Bo Keun Park, Gun Hwan Kim, Dong Ju Jeon, Taek-Mo Chung, Jeong Hwan Han



PII: S0272-8842(18)32745-7  
DOI: <https://doi.org/10.1016/j.ceramint.2018.09.263>  
Reference: CERI19662

To appear in: *Ceramics International*

Received date: 22 August 2018  
Revised date: 18 September 2018  
Accepted date: 26 September 2018

Cite this article as: Hyo Yeon Kim, Ji Hyeun Nam, Sheby Mary George, Jin-Seong Park, Bo Keun Park, Gun Hwan Kim, Dong Ju Jeon, Taek-Mo Chung and Jeong Hwan Han, Phase-controlled SnO<sub>2</sub> and SnO Growth by Atomic Layer Deposition using Bis(*N*-ethoxy-2,2-dimethyl propanamido)tin Precursor, *Ceramics International*, <https://doi.org/10.1016/j.ceramint.2018.09.263>

This is a PDF file of an unedited manuscript that has been accepted for publication. As a service to our customers we are providing this early version of the manuscript. The manuscript will undergo copyediting, typesetting, and review of the resulting galley proof before it is published in its final citable form. Please note that during the production process errors may be discovered which could affect the content, and all legal disclaimers that apply to the journal pertain.

Phase-controlled SnO<sub>2</sub> and SnO Growth by Atomic Layer Deposition using  
Bis(*N*-ethoxy-2,2-dimethyl propanamido)tin Precursor

Hyo Yeon Kim,<sup>a,b</sup> Ji Hyeun Nam,<sup>a</sup> Sheby Mary George,<sup>a</sup> Jin-Seong Park,<sup>b</sup> Bo Keun Park,<sup>a,c</sup> Gun  
Hwan Kim,<sup>a</sup> Dong Ju Jeon,<sup>a</sup> Taek-Mo Chung,<sup>a,c</sup> and Jeong Hwan Han<sup>a,d,\*</sup>

<sup>a</sup>*Division of Advanced Materials, Korea Research Institute of Chemical Technology(KRICT),  
141 Gajeong-Ro, Yuseong-Gu, Daejeon, 34114, Republic of Korea*

<sup>b</sup>*Division of Materials Science and Engineering, Hanyang University, 222 Wangsimni-Ro, Seoul  
04763, Republic of Korea*

<sup>c</sup>*Department of Chemical Convergence Materials, University of Science and Technology (UST),  
217, Gajeong-Ro, Yuseong-Gu, Deajeon 34113, Republic of Korea*

<sup>d</sup>*Department of Materials Science and Engineering, Seoul National University of Science and  
Technology, Seoul 01811, Republic of Korea*

*\*E-mail: jhan@seoultech.re.kr*

**Abstract**

Atomic layer deposition (ALD) of SnO and SnO<sub>2</sub> thin films was successfully demonstrated over a wide temperature range of 70–300 °C using a divalent Sn-precursor, bis(*N*-ethoxy-2,2-dimethyl propanamido)tin (Sn(edpa)<sub>2</sub>). The regulated growth of the SnO<sub>2</sub> and SnO films was realized by employing O<sub>2</sub>-plasma and H<sub>2</sub>O, respectively. Pure SnO<sub>2</sub> and SnO films were deposited with negligible C and N contents at all the growth temperatures, and the films exhibited polycrystalline and amorphous structures, respectively. The SnO<sub>2</sub> films presented a high transmittance of > 85% in the wavelength range of 400–700 nm and an indirect band gap of 3.6–4.0 eV; meanwhile, the SnO films exhibited a lower transmittance of > 60% and an indirect band gap of 2.9–3.0 eV. The SnO<sub>2</sub> films exhibited n-type semiconducting characteristics with carrier concentrations of  $8.5 \times 10^{16}$ – $1.2 \times 10^{20}$  cm<sup>-3</sup> and Hall mobilities of 2–26 cm<sup>2</sup>/V·s. By employing an alternate ALD growth of SnO and SnO<sub>2</sub> films, SnO<sub>2</sub>/SnO multilayer structures were successfully fabricated at 120 °C. The in-situ quadrupole mass spectrometry analysis performed during ALD revealed that the oxidation of chemisorbed Sn-precursor occurs dominantly during the Sn(edpa)<sub>2</sub>/O<sub>2</sub>-plasma ALD process, resulting in the production of combustion by-products, whereas the Sn(edpa)<sub>2</sub>/H<sub>2</sub>O ALD process was governed by a ligand exchange reaction with the maintenance of the original oxidation state of Sn<sup>2+</sup>.

Keyword: SnO<sub>2</sub>, SnO, atomic layer deposition, bis(*N*-ethoxy-2,2-dimethyl propanamido)tin, quadrupole mass spectrometer

## Introduction

Binary oxide semiconductors of the Sn–O system, such as SnO<sub>2</sub> and SnO, have been extensively investigated owing to their versatile applications in displays [1-3], gas sensors [4,5], photocatalysts [6,7], transparent electronics [8,9], and optoelectronics [10,11]. Owing to the different oxidation states (+4 and +2) of the Sn cation, the SnO<sub>2</sub> and SnO films exhibit distinctive optical, chemical, and electrical properties. SnO<sub>2</sub> is an n-type semiconducting oxide with an electron concentration level of  $10^{18}$ – $10^{21}$  cm<sup>-3</sup>, and the formation of excess electrons is attributed to the presence of intrinsic point defects such as the oxygen vacancy or Sn interstitial in SnO<sub>2</sub> [12-14]. The largely overlapped spherical 5s orbitals in SnO<sub>2</sub> enables the facile transport of electrons in the conduction band, resulting in properties exhibiting high potential, including a high electron mobility and low resistivity [14]. Meanwhile, SnO generally exhibits a p-type semiconductor nature owing to the presence of intrinsic Sn vacancies or oxygen interstitials. First-principle calculations revealed that Sn vacancies mainly contribute to hole conduction by forming unoccupied states near the valence band maximum [15,16]. Owing to its remarkable hole transport property, a high field effect mobility of 0.13–6.75 cm<sup>2</sup>/V·s has been achieved from SnO-based p-channel thin film transistors (TFTs) [3,17-19].

Recently, as the demand for realizing complementary circuit devices based on oxide semiconductors has increased, the growth processes of n-type SnO<sub>2</sub> films as well as p-type SnO films have received significant attention. The growth of n-type SnO<sub>2</sub> film has been extensively conducted using various vacuum deposition processes such as sputtering [20], evaporation [21], chemical vapor deposition [22,23], and atomic layer deposition (ALD) [24-30]. Among these methods, ALD exhibits superior advantages for producing physically and chemically uniform films on large and complex substrates owing to its unique self-limiting deposition behavior. For

decades, various combinations of Sn-precursor and reactant have been explored for performing ALD of  $\text{SnO}_2$ . Sn-halides such as  $\text{SnCl}_4$  and  $\text{SnI}_4$  were used for producing highly pure polycrystalline  $\text{SnO}_2$  films; however, high deposition temperatures in the range of 300–750 °C are required owing to the insufficient reactivity of Sn-halide precursors [24,25]. In addition, Sn-halide precursors form corrosive by-products such as HCl, which deteriorates the resultant film properties. Meanwhile, the adoption of metal–organic Sn-precursors for ALD of  $\text{SnO}_2$  enabled the growth of high-quality  $\text{SnO}_2$  films at relatively lower deposition temperatures (< 300 °C). Tetrakis(dimethylamido)tin(IV) (TDMASn) has been commonly used for producing  $\text{SnO}_2$  films by ALD, and the use of different reactants such as  $\text{H}_2\text{O}$ ,  $\text{H}_2\text{O}_2$ , and  $\text{O}_3$  has been explored [26–28]. ALD using TDMASn/ $\text{H}_2\text{O}$  resulted in  $\text{SnO}_2$  film with a growth rate of 0.06–0.07 nm/cycle at 100–200 °C, whereas the use of TDMASn/ $\text{O}_3$  and TDMASn/ $\text{H}_2\text{O}_2$  resulted in enhanced  $\text{SnO}_2$  growth rates of 0.09–0.13 nm/cycle owing to the higher reactivity of  $\text{H}_2\text{O}_2$  and  $\text{O}_3$  compared to  $\text{H}_2\text{O}$ . Regardless of the reactant type, n-type  $\text{SnO}_2$  films were obtained from TDMASn. Dibutyltin(IV)-diacetate (DBTA) and tin(IV)-butoxide were used as Sn-precursors in the plasma-enhanced ALD (PEALD) process at deposition temperatures of 200–400 °C to obtain pure  $\text{SnO}_2$  films suitable for gas sensor and Li-ion battery applications [29,30].

In contrast to n-type  $\text{SnO}_2$ , very limited success has been achieved in the fabrication of p-type SnO and its applications. Most of the studies on the growth of SnO film employed physical vapor deposition (PVD) methods such as reactive sputtering and reactive evaporation under delicately regulated process conditions with respect to the process pressure, partial pressure of oxidative or reductive gases, and deposition temperature [17,31]. This is because SnO is metastable and can be straightforwardly oxidized to  $\text{SnO}_2$  or decomposed to  $\text{SnO}_2$  and Sn metal by a disproportionation reaction [32]. Therefore, an alternate method for producing pure SnO films with a wide and stable process window should be developed. We reported the successful growth of pure SnO for the first time by ALD using bis(dimethylamino-2-methyl-2-propoxy)tin(II) ( $\text{Sn}(\text{dmamp})_2$ ) and  $\text{H}_2\text{O}$  [33]. Polycrystalline SnO films exhibiting p-type

conductivity were obtained at 150–210 °C. Furthermore, the ALD-grown SnO film obtained from Sn(dmamp)<sub>2</sub>/H<sub>2</sub>O exhibited remarkable p-channel TFT performances with a high field effect mobility of ~1 cm<sup>2</sup>/V·s and I<sub>on</sub>/I<sub>off</sub> ratio of ~2 × 10<sup>6</sup> [34].

In this study, we conducted ALD growth of SnO<sub>2</sub> and SnO films using an Sn-precursor, bis(*N*-ethoxy-2,2-dimethyl propanamido)tin (Sn(edpa)<sub>2</sub>); moreover, the phase of the SnO<sub>x</sub> films, SnO<sub>2</sub> and SnO, was effectively controlled by employing different reactants, namely, O<sub>2</sub>-plasma and H<sub>2</sub>O, respectively. The surface reactions during the SnO<sub>2</sub> and SnO ALD processes were investigated by employing in-situ mass spectrometric residual gas analysis. Furthermore, ex-situ analyses on the chemical, physical, optical, and electrical properties as well as microstructures of the SnO<sub>2</sub> and SnO films were performed.

## Experimental Section

ALD of SnO<sub>2</sub> and SnO was carried out in a 4-inch showerhead type reactor (ForALL, Korea) on Si and quartz substrates at deposition temperatures within 70–300 °C. The base pressure and process pressure during the ALD process were 20 mTorr and 1–1.5 Torr, respectively. The Sn(edpa)<sub>2</sub> precursor was synthesized on lab scale and employed for growing both SnO<sub>2</sub> and SnO films. As shown in Fig. S1a, Sn(edpa)<sub>2</sub> is a homoleptic metal-organic complex with the central Sn(II) atom tetra-coordinated by two edpa chelating ligands. As two of the four neighboring oxygen atoms form ionic bonds with the central atom and the others form coordinate bonds, Sn(edpa)<sub>2</sub> exhibits divalent rather than tetravalent characteristics. The detailed synthetic procedure and characteristics of Sn(edpa)<sub>2</sub> have been reported previously [35]. During ALD, Sn(edpa)<sub>2</sub> was kept in a canister at 60 °C and delivered into the reactor with an Ar carrier gas flow of 100 standard cubic centimeters per minute (sccm). The precursor delivery line was heated to 75 °C during the deposition process. For fabricating the SnO<sub>2</sub> and SnO films, O<sub>2</sub>-plasma and H<sub>2</sub>O, respectively, were introduced as reactants. O<sub>2</sub>-plasma was generated with an

oxygen flow of 100 sccm at the plasma power of 100 W. The canister for H<sub>2</sub>O was maintained at 25 °C, and the H<sub>2</sub>O vapor was introduced into the chamber without any carrier gas. A cycle of the ALD process consisted of four sequential steps; (1) Sn(edpa)<sub>2</sub> pulse, (2) Ar purge (500 sccm), (3) reactant gas pulse (O<sub>2</sub>-plasma or H<sub>2</sub>O), and (4) Ar purge (500 sccm). To remove the excess Sn-precursor and reactant as well as by-products, Ar purge gas was introduced for 10 s and 15 s for the O<sub>2</sub>-plasma- and H<sub>2</sub>O-based process, respectively.

The thickness, refractive index, and extinction coefficient (*k*) of the ALD deposited SnO<sub>2</sub> and SnO films were measured by spectroscopic ellipsometry in the wavelength range of 275–826 nm (SE, Horiba scientific, UVISSEL). The chemical binding properties and O/Sn composition ratios of the SnO<sub>2</sub> and SnO films were examined using X-ray photoelectron spectroscopy (XPS, Thermo Scientific, K-alpha) with Al K $\alpha$  monochromatic X-ray source. The photoelectrons were collected at an analyzer pass energy of 50 eV and a photoelectron take-off angle of 0°. For XPS depth profile analysis, the deposited films were sputtered with an Ar<sup>+</sup> ion beam at 2 keV. The Advantage software was used for spectral deconvolution and depth profiling. To reveal the crystallinity of the SnO<sub>2</sub> and SnO films, glancing angle X-ray diffraction (GAXRD, Rigaku, smartlab) was employed at the incident X-ray angle of 1°. The topography of the SnO<sub>x</sub> film surfaces was measured by atomic force microscopy (AFM, DI-3100, Veeco). Atomic-scale crystallographic examinations of the SnO<sub>2</sub>/SnO multilayer structure fabricated on the TiN substrate were performed using high-resolution transmission electron microscopy (HRTEM, JEM-2100F, JEOL LTD.). The transmittance of the films in visible light was measured using UV–Vis spectroscopy (Shimadzu, UV-1800). The electrical properties of the deposited films were examined using Hall measurements.

For in-situ analysis of the surface chemical reaction during the SnO<sub>2</sub> and SnO ALD processes, a quadrupole mass spectrometer (QMS, Balzers, ABB Extrel MEXM-1000) was connected to the deposition system. The reaction by-products were collected through the capillary line and

ionized by electron bombardment at 1 KeV. The time-resolved by-product signals with different mass-to-charge ratios ( $m/z$ ) of 30, 44, 57, and 146 corresponding to NO, CO<sub>2</sub>, <sup>t</sup>Bu, and edpaH, respectively, were detected using a secondary electron multiplier.

## Results and Discussion

The self-limited reaction of the Sn(edpa)<sub>2</sub>/O<sub>2</sub>-plasma and Sn(edpa)<sub>2</sub>/H<sub>2</sub>O ALD processes was examined at a growth temperature of 120 °C by increasing the Sn-precursor and reactant pulse times. As shown in Fig. 1a, the Sn(edpa)<sub>2</sub>/O<sub>2</sub>-plasma PEALD process exhibited a saturated growth behavior at Sn(edpa)<sub>2</sub> and O<sub>2</sub>-plasma pulse-lengths of over 10 and 5 s, respectively. A saturated growth rate of ~0.07 nm/cycle was achieved, which is comparable to that obtained for TDMASn/H<sub>2</sub>O ALD [26,27]. For Sn(edpa)<sub>2</sub>/H<sub>2</sub>O, a self-saturated surface reaction occurred with Sn(edpa)<sub>2</sub> and H<sub>2</sub>O pulse lengths of over 10 and 1 s, respectively (Fig. 1b). As compared to the Sn(edpa)<sub>2</sub>/O<sub>2</sub>-plasma process, a significantly lower growth rate of 0.026 nm/cycle was obtained for the Sn(edpa)<sub>2</sub>/H<sub>2</sub>O process; this may be ascribed to the lower reactivity of H<sub>2</sub>O. The change in the growth rate achieved with both the ALD processes as a function of the deposition temperature was examined in the growth temperature range of 70–300 °C (Fig. 1c). The SnO<sub>2</sub> and SnO ALD processes were conducted at various temperatures with fixed pulse conditions of 12 s (Sn-precursor)–10 s (Ar purge)–5 s (O<sub>2</sub>-plasma)–5 s (Ar purge) and 12 s (Sn-precursor)–15 s (Ar purge)–2 s (H<sub>2</sub>O)–5 s (Ar purge), respectively. For the Sn(edpa)<sub>2</sub>/O<sub>2</sub>-plasma PEALD process, a constant growth rate of 0.07 nm/cycle was achieved at the ALD temperature window of 70–180 °C. Above 180 °C, the growth rate increased with an increase in the deposition temperature. This increase in the growth rate may be ascribed to the limited thermal stability of the Sn(edpa)<sub>2</sub> precursor. The thermal stability of the Sn(edpa)<sub>2</sub> precursor was examined by introducing only the Sn-precursor into the reactor at elevated stage temperatures of 90–300 °C (Fig. S1b). The Sn layer density on the Si substrate examined by XRF started to increase rapidly



from 180 °C, indicating the onset of thermal decomposition of  $\text{Sn}(\text{edpa})_2$ . The NMR spectra of the  $\text{Sn}(\text{edpa})_2$  precursor exhibit results consistent with those obtained by XRF (Fig. S1c). As compared to the NMR spectrum of pristine  $\text{Sn}(\text{edpa})_2$ , a different NMR spectrum was obtained when  $\text{Sn}(\text{edpa})_2$  was maintained at a high temperature of 200 °C for 1 d. This is likely to be owing to the thermal decomposition of  $\text{Sn}(\text{edpa})_2$  occurring at approximately 200 °C. The  $\text{Sn}(\text{edpa})_2/\text{H}_2\text{O}$  ALD process exhibited an almost constant growth rate of 0.026 nm/cycle at all the investigated temperatures (70–300 °C) notwithstanding the limited thermal stability of  $\text{Sn}(\text{edpa})_2$  above 200 °C. The discrepancy in the temperature dependence of the growth rate between the  $\text{Sn}(\text{edpa})_2/\text{O}_2$ -plasma and  $\text{Sn}(\text{edpa})_2/\text{H}_2\text{O}$  processes may be attributed to the formation of different surface species after the  $\text{O}_2$ -plasma and  $\text{H}_2\text{O}$  pulse steps. Generally, in the  $\text{O}_2$ -plasma-assisted PEALD, both surface hydroxyl and carbonate groups are formed as reactive sites for the chemisorption of incoming metal-precursors, whereas the  $\text{H}_2\text{O}$ -based ALD process predominantly generates surface OH groups [36]. Accordingly, it is presumed that the rapid increase in the growth rate in the  $\text{Sn}(\text{edpa})_2/\text{O}_2$ -plasma PEALD process over 200 °C is owing to the higher reactivity of the partially decomposed Sn-precursor with the carbonate surface groups than with the OH surface. The refractive indexes of the resultant  $\text{SnO}_x$  films were measured by fitting the SE results using the Adachi–Forouhi dispersion model, as shown in Fig. 1d. Luo et al. reported a change in the refractive index of  $\text{SnO}_x$  films from 3.0 to 1.8 as the phase of the film varied from SnO to  $\text{SnO}_2$  [37]. The refractive index (at a wavelength of 550 nm) of the films deposited by  $\text{Sn}(\text{edpa})_2/\text{O}_2$ -plasma PEALD was 1.9–2.0 at all the deposition temperatures, which is reasonably consistent with that of the reported values for the  $\text{SnO}_2$  films. However, the films grown with  $\text{Sn}(\text{edpa})_2/\text{H}_2\text{O}$  exhibited a higher refractive index of 2.7–2.8, which is close to that obtained for the SnO phase [37].

To further reveal the phase of the deposited  $\text{SnO}_x$  films and its chemical properties depending on the selection of the co-reactant, XPS surface and depth profiling analysis were conducted, as depicted in Figs. 2a–c. Figure 2a shows the normalized Sn 3d spectra for the  $\text{SnO}_x$  films

deposited using O<sub>2</sub>-plasma or H<sub>2</sub>O at different reactor temperatures. With Sn(edpa)<sub>2</sub>/O<sub>2</sub>-plasma, the Sn 3d<sub>5/2</sub> spectra exhibited a peak centered at 486.7–486.8 eV irrespective of the growth temperatures, indicating the Sn oxidation state to be +4. The Sn 3d<sub>5/2</sub> sub-peak corresponding to the Sn<sup>2+</sup> chemical state (~486.2 eV) was not observed. This implies that Sn cation with an oxidation state of +2 in pristine Sn(edpa)<sub>2</sub> is completely converted to Sn<sup>4+</sup> during the O<sub>2</sub>-plasma-based PEALD process because of the strong oxidation power of O<sub>2</sub>-plasma, resulting in the formation of the SnO<sub>2</sub> film. With the Sn(edpa)<sub>2</sub>/H<sub>2</sub>O process, the peak positions in the Sn 3d<sub>5/2</sub> spectra shifted to marginally lower binding energy values of 486.2–486.3 eV irrespective of the deposition temperatures. This is ascribed to the formation of SnO by maintaining the original oxidation state of +2. The broader Sn 3d<sub>5/2</sub> XP spectra width achieved for the SnO film is likely to have resulted from the marginal presence of the Sn<sup>4+</sup> oxidation state, as evident from the weak sub-peaks observed at ~486.7 eV as well as the structural disorder of amorphous SnO. In addition, the O 1s XP spectra of the deposited were examined (Fig. S2). The O 1s XP spectra result is consistent with the Sn 3d XP spectra in that O-Sn<sup>4+</sup> and O-Sn<sup>2+</sup> binding states were formed using Sn(edpa)<sub>2</sub>/O<sub>2</sub>-plasma and Sn(edpa)<sub>2</sub>/H<sub>2</sub>O precursor combinations, respectively. The structural property of the deposited films will be discussed later. To examine the atomic composition profiles of the deposited films, the XPS depth profiling of the SnO<sub>2</sub> and SnO films grown at 120 °C was examined, and the results are shown in Figs. 2b and c, respectively. The SnO<sub>2</sub> film grown with the O<sub>2</sub>-plasma-based PEALD exhibited an O/Sn ratio of 1.2 and a uniform O/Sn distribution in the depth direction. The SnO<sub>2</sub> films grown at 120 °C contained negligible C and N impurities. In contrast, the SnO film formed with H<sub>2</sub>O as the reactant exhibited a significantly lower O/Sn ratio of 0.74. The significant difference between the O/Sn ratios of the films achieved with Sn(edpa)<sub>2</sub>/O<sub>2</sub>-plasma and Sn(edpa)<sub>2</sub>/H<sub>2</sub>O indicates the remarkable phase controllability of the SnO<sub>x</sub> ALD processes carried out in this study. It should be noted that the absolute O/Sn ratio determined by XPS quantitative analysis is not very accurate even after considering the atomic sensitivity factors of each element. In Fig. 2c, the gradual decrease in the O/Sn ratio with the increase in the Ar sputtering time is because of the

preferential oxygen loss from SnO occurring during sputtering, rather than the non-uniform distributions of O and Sn. The XPS depth profiles of the  $\text{SnO}_x$  films deposited at the different temperatures are shown in Fig. S3. The O/Sn ratios as well as the impurity level of the  $\text{SnO}_2$  and SnO films were not strongly affected by the growth temperature.

The crystallinity of the  $\text{SnO}_2$  and SnO films grown on Si substrates was investigated by ex-situ GAXRD. Figure 3a shows the diffraction patterns of the  $\text{SnO}_2$  films deposited at various temperatures within 70–300 °C. At a low temperature of  $\geq 70$  °C, the deposited films exhibited peaks corresponding to polycrystalline  $\text{SnO}_2$ , with the diffraction peaks observed at 26.6° [ $\text{SnO}_2$  (110)], 33.9° [ $\text{SnO}_2$  (101)], and 38.2° [ $\text{SnO}_2$  (200)]. The growth of polycrystalline and pure  $\text{SnO}_2$  below 100 °C appears to exhibit potential in terms of the application of temperature-damageable substrates such as plastics, textiles, and biomaterials. Within an ALD temperature window of 70–120 °C, a strong (101) preferred orientation was observed, whereas the films deposited at 220–300 °C exhibited a randomly oriented  $\text{SnO}_2$  structure. At 70 and 120 °C, no other phase (e.g., metallic Sn, SnO, and  $\text{SnO}_{2-x}$ ) were detected, indicating the formation of a pure  $\text{SnO}_2$  film. Beyond the ALD temperature window of 220 and 300 °C, a diffraction peak was observed at 24.7°, which may be attributed to the oxygen deficient  $\text{SnO}_{2-x}$  phase [38]. The SnO films obtained from  $\text{Sn}(\text{edpa})_2/\text{H}_2\text{O}$  are in the nanocrystalline or amorphous state as-deposited at all the temperatures, as presented in Fig. 3b. In contrast to the amorphous n-type oxide semiconductor such as  $\text{SnO}_2$ , ZnSnO, and InGaZnO, the amorphous structure of p-type SnO is unfavorable for applications in p-channel TFTs because the hybridization of O 2p orbital with Sn 5s orbital results in a hole conduction pathway with a directional property. Considering that the polycrystalline ALD SnO films were achieved using  $\text{Sn}(\text{dmamp})_2/\text{H}_2\text{O}$  above 150 °C [33], the reason for the formation of the amorphous SnO films upon using  $\text{Sn}(\text{edpa})_2$  is as of yet clear; however, it could be closely related to the different ligand structures of  $\text{Sn}(\text{edpa})_2$  and  $\text{Sn}(\text{dmamp})_2$ . Amorphous-like SnO film grown at 120 °C was annealed at 450 °C in  $\text{N}_2$  ambient. Thereafter, the crystalline property was examined by XRD, as shown in Fig. 3c. The

film exhibited evident diffraction peak corresponding to polycrystalline SnO (001) and (002) planes, indicating that the polycrystalline SnO film was formed after the annealing process.

Figure 4 shows the surface topography of ~20 nm-thick SnO<sub>2</sub> and SnO films scanned by AFM. As shown in Figs. 4a and b, as-deposited SnO<sub>2</sub> films at 120 and 220 °C by Sn(edpa)<sub>2</sub>/O<sub>2</sub>-plasma process exhibited grain-like morphology with RMS roughness values of 1.2 and 1.7 nm, respectively. Meanwhile, the topography of the SnO films from the Sn(edpa)<sub>2</sub>/H<sub>2</sub>O ALD with RMS roughness of 0.2–0.3 nm appears to be significantly smoother than those of the SnO<sub>2</sub> films. This is likely to be owing to the amorphous (or nanocrystalline) nature of the as-deposited SnO film (Figs. 4c–e). As depicted in Fig. 4f, after 450 °C N<sub>2</sub> annealing, the SnO film exhibited a crystallized structure with an enlarged grain size of 100–200 nm. After post annealing, the poly-crystallized SnO film matches reasonably with the XRD observation shown in Fig. 3c.

The optical band gap of the SnO<sub>x</sub> films was measured using the Tauc plot ( $\alpha h\nu$  vs  $h\nu^{1/n}$ , where  $\alpha$  is the absorption coefficient calculated as  $2\pi k/\lambda$ , and  $n$  values of 1/2 were used for estimating the indirect band gap). As shown in Figs. 5a and b, optical interband absorptions were observed in the SnO<sub>2</sub> and SnO films. The direct band gap of the SnO<sub>2</sub> films was in the range of 3.6–4.0 eV, which is reasonably consistent with the values achieved with other deposition techniques such as sputtering and pulse laser deposition [39,40]. The SnO<sub>2</sub> films deposited at 70–220 °C exhibited a marginally stronger band-tail near the band edge as compared to that deposited at 300 °C. In contrast, the amorphous SnO films exhibited lower indirect band gap energy values (in the range of 2.9–3.0 eV). Accordingly, distinct transmittance features were observed with the SnO<sub>2</sub> and SnO films in visible light, as shown in Fig. 5c. The SnO<sub>2</sub> film grown at 120 °C was highly transparent in the range of 400–700 nm (> 85%), whereas the SnO film exhibited a lower transmittance of > 60%.

To evaluate the electrical properties of the SnO<sub>2</sub> and SnO films, Hall measurements were performed, as depicted in Fig. 6. The SnO<sub>2</sub> film exhibited a negative Hall coefficient, indicating

an n-type carrier conduction. The carrier concentration of the SnO<sub>2</sub> films increased dramatically (from  $8.5 \times 10^{16}$  to  $1.2 \times 10^{20}$  cm<sup>-3</sup>) with an increase in the growth temperature from 120 to 300 °C. The resistivity of the SnO<sub>2</sub> films changed significantly (from  $3 \times 10^1$  to  $4 \times 10^{-3}$  Ω·cm) with an increase in the growth temperature, which may be ascribed to the increased carrier concentration and crystallinity achieved at high growth temperatures. Hall mobilities of 2–26 cm<sup>2</sup>/V·s were achieved, with the highest value of 26 cm<sup>2</sup>/V·s at a deposition temperature of 220 °C. The Hall measurement results obtained from the 70 °C-grown SnO<sub>2</sub> film was not reliable owing to its high resistivity. We could not obtain reproducible results with the SnO film, probably owing to the ineffective hole transport property and high film resistivity of the SnO films.

As verified previously, the SnO<sub>x</sub> ALD processes in this study provide a reasonable phase (composition)-controllability between SnO<sub>2</sub> and SnO. Therefore, a nanolaminate film composed of alternate amorphous SnO and polycrystalline SnO<sub>2</sub> layers was fabricated on a TiN substrate at 120 °C. 210 cycles of SnO<sub>2</sub> PEALD followed by 580 cycles of SnO ALD were repeated three times to produce the laminate structure shown in Fig. 7a. The thicknesses of the SnO<sub>2</sub> and SnO films were approximately 16 and 15 nm, respectively. In the bright field TEM image, each layer is clearly distinguished owing to the difference in the O/Sn composition ratio and the degree of diffraction contrast of the polycrystalline SnO<sub>2</sub> and amorphous SnO layers. The XPS depth profile shown in Fig. 7b reveals a periodic change in the Sn and O atomic percentage, indicating the successful growth of SnO<sub>2</sub> on SnO and vice versa. The HRTEM image of the sample recorded near the SnO<sub>2</sub>/SnO interface (Fig. 7c) indicates the formation of an amorphous (with partial nanocrystalline) SnO film on the polycrystalline SnO<sub>2</sub> film. SnO<sub>2</sub> (101) and (110) lattice planes with a d-spacing of 0.26 and 0.33 nm, respectively, are clearly visible on the SnO<sub>2</sub> layer, which is reasonably consistent with the XRD results. The fast Fourier transform (FFT) patterns of the marked areas shown in Fig. 7c indicated the polycrystalline and amorphous natures of the SnO<sub>2</sub> and SnO films, respectively.

The surface reaction mechanisms of the SnO<sub>2</sub> and SnO formation by ALD were investigated by in-situ QMS at 120 °C. During the QMS analysis, the ALD processes were conducted using modified pulse conditions of 12 s (Sn(edpa)<sub>2</sub>)–60 s (Ar purge)–5 s (O<sub>2</sub>-plasma or H<sub>2</sub>O)–60 s (Ar purge). Sufficient Ar purge time (60 s) was used to ensure that the achieved QMS signals are obtained as a result of surface reaction rather than gas phase reaction. According to the reports on the surface reaction of oxide ALDs, various types of by-product gases are likely to be obtained from both the ALD processes: namely, edpaH<sup>+</sup> ( $m/z = 145$ ) from a ligand exchange reaction and CO<sub>2</sub><sup>+</sup> ( $m/z = 44$ ), NO<sup>+</sup> ( $m/z = 30$ ), and H<sub>2</sub>O<sup>+</sup> ( $m/z = 18$ ) from a combustion reaction. Figure 8a shows the change in the intensity of the  $m/z = 44$  signal achieved during an ALD cycle of both the SnO<sub>2</sub> and SnO deposition processes. For the SnO<sub>2</sub> PEALD, a sharp  $m/z = 44$  signal was observed at the O<sub>2</sub>-plasma pulse step, whereas no signal was observed during the Sn-precursor step. This indicates the production of CO<sub>2</sub> gas by the combustion of edpa ligands only at the O<sub>2</sub>-plasma pulse step. The  $m/z = 44$  signal attained the maximum intensity in a short time of 1 s, after which it started to decrease rapidly. This implies a high combustion rate of the absorbed Sn-precursor at the O<sub>2</sub>-plasma step. However, there is a negligible CO<sub>2</sub> formation during the SnO ALD process at both the Sn-precursor and H<sub>2</sub>O pulse steps, indicating that the surface reaction during the SnO ALD does not involve a combustion reaction. The inset in Fig. 8a shows the variation of the  $m/z = 30$  signal, verifying the formation of NO<sub>x</sub> species because the Sn(edpa)<sub>2</sub> precursor contains N atoms in the ligand. Analogous to the CO<sub>2</sub> signal observed during the SnO<sub>2</sub> PEALD, a strong peak was observed only at the O<sub>2</sub>-plasma pulse step, indicating the production of NO by ligand combustion. Although there was a marginal increase in the intensity of the  $m/z = 30$  signal for the case of SnO ALD, it may be attributed to the fragmentation of the edpa ligands and not to a NO reaction by-product.

To examine the release of ligands, the signals corresponding to edpaH<sup>+</sup> ( $m/z = 145$ ) and <sup>t</sup>Bu<sup>+</sup> ( $m/z = 57$ , one of the dissociative fragments of edpaH) were analyzed as shown in Fig. 8b. As depicted in the inset of Fig. 8b, the parent edpaH<sup>+</sup> signal could not be detected, probably

because of the cracking of the edpaH ligand by electron ionization. Hence, we analyzed its highest fragment peak at  $m/z = 57$  [35]. For the SnO ALD, a signal corresponding to  $t\text{Bu}^+$  was observed at both the Sn-precursor and  $\text{H}_2\text{O}$  pulse steps, indicating the release of complete edpaH ligands as a result of a ligand exchange reaction. The release of edpaH during the SnO ALD is likely because the ALD growth of oxide films in the presence of  $\text{H}_2\text{O}$  as the reactant is generally known to involve H-transfer reaction and hydrolysis reaction at the metal-precursor and  $\text{H}_2\text{O}$  pulse steps, respectively [41,42]. It is noteworthy that the evidence for the release of edpaH was observed in the  $\text{SnO}_2$  PEALD process notwithstanding the absence of  $\text{H}_2\text{O}$  as the reactant. This is likely to have been caused by the formation of  $\text{H}_2\text{O}$  as a by-product during the  $\text{O}_2$ -plasma pulse step, which functions as a reactant along with  $\text{O}_2$ -plasma.

## Conclusion

ALD processes of  $\text{SnO}_2$  and SnO films were successfully developed by employing  $\text{Sn}(\text{edpa})_2$  as the Sn-precursor and  $\text{O}_2$ -plasma or  $\text{H}_2\text{O}$  as the reactant. The  $\text{SnO}_2$  and SnO films were obtained with remarkable phase controllability, which is facilitated by different surface reaction mechanisms of the  $\text{Sn}(\text{edpa})_2/\text{O}_2$ -plasma and  $\text{Sn}(\text{edpa})_2/\text{H}_2\text{O}$  processes. Combustion and ligand exchange reactions occur with  $\text{SnO}_2$  and SnO ALD, respectively. Impurity-free films were obtained even at relatively low growth temperatures of 70–180 °C. The as-deposited  $\text{SnO}_2$  films obtained with  $\text{O}_2$ -plasma exhibited a polycrystalline structure, whereas amorphous SnO films were obtained at all the investigated temperatures. The optical band gaps of  $\text{SnO}_2$  and SnO films were measured to be 3.6–4.0 and 2.9–3.0 eV, respectively. Sequential depositions of  $\text{SnO}_2$  and SnO films resulted in the formation of an  $\text{SnO}_2/\text{SnO}$  multilayer heterojunction with an evident phase distinction between the  $\text{SnO}_2$  and SnO layers. The phase controlled ALD growth of  $\text{SnO}_2$  and SnO films in this study exhibits high potential for utilization for various applications such as TFTs, gas/photo sensors, photovoltaics, and catalysts.

## Acknowledgements

This work was supported by Korea Research Institute of Chemical Technology (SI1803, Development of smart chemical materials for IoT device) and by the Research fund provided for a new professor by SeoulTech (Seoul National University of Science and Technology).

## References

- [1] E.N. Dattoli, Q. Wan, W. Guo, Y. Chen, X. Pan, W. Lu, Fully Transparent Thin-Film Transistor Devices Based on SnO<sub>2</sub> Nanowires, *Nano Lett.* 7 (2007) 2463.
- [2] J. Jang, R. Kitsomboonloha, S.L. Swisher, E.S. Park, H. Kang, V. Subramanian, Transparent High-Performance Thin Film Transistors from Solution-Processed SnO<sub>2</sub>/ZrO<sub>2</sub> Gel-like Precursors, *Adv. Mater.* 25 (2013) 1042.
- [3] Y. Ogo, H. Hiramatsu, K. Nomura, H. Yanagi, T. Kamiya, M. Hirano, H. Hosono, P-channel Thin-film Transistor using P-type Oxide Semiconductor, SnO, *Appl. Phys. Lett.* 93 (2008) 032113.
- [4] B. Wang, L.F. Zhu, Y.H. Yang, N.S. Xu, G.W. Yang, Fabrication of a SnO<sub>2</sub> Nanowire Gas Sensor and Sensor Performance for Hydrogen, *J. Phys. Chem. C* 112 (2008) 6643.
- [5] Q. Kuang, C. Lao, Z.L. Wang, Z. Xie, L. Zheng, High-Sensitivity Humidity Sensor Based on a Single SnO<sub>2</sub> Nanowire, *J. Am. Chem. Soc.* 129 (2007) 6070.
- [6] A.K. Sinha, P.K. Manna, M. Pradhan, C. Mondal, S.M. Yusuf, T. Pal, Tin Oxide with a p-n



Heterojunction Ensures both UV and Visible Light Photocatalytic Activity, RSC Adv. 4 (2014) 208.

[7] Y.C. Zhang, Z.N. Du, K.W. Li, M. Zhang, D.D. Dionysiou, High-Performance Visible-Light-Driven  $\text{SnS}_2/\text{SnO}_2$  Nanocomposite Photocatalyst Prepared via In situ Hydrothermal Oxidation of  $\text{SnS}_2$  Nanoparticles, ACS Appl. Mater. Interfaces 3 (2011) 1528.

[8] Dhananjay, C.-W. Chu, C.-W. Ou, M.-C. Wu, Z.-Y. Ho, K.-C. Ho, S.-W. Lee, Complementary Inverter Circuits based on p- $\text{SnO}_2$  and n- $\text{In}_2\text{O}_3$  Thin Film Transistors, Appl. Phys. Lett. 92 (2008) 232103.

[9] Z. Wang, H.A. Al-Jawhari, P.K. Nayak, J.A. Caraveo-Frescas, N. Wei, M.N. Hedhili, H.N. Alshareef, Low Temperature Processed Complementary Metal Oxide Semiconductor (CMOS) Device by Oxidation Effect from Capping Layer, Sci. Rep. 5 (2015) 9617.

[10] W. Ke, G. Fang, Q. Liu, L. Xiong, P. Qin, H. Tao, J. Wang, H. Lei, B. Li, J. Wan, G. Yang, Y. Yan, Low-Temperature Solution-Processed Tin Oxide as an Alternative Electron Transporting Layer for Efficient Perovskite Solar Cells, J. Am. Chem. Soc. 137 (2015) 6730.

[11] S. Trost, A. Behrendt, T. Becker, A. Polywka, P. Görrn, T. Riedl, Tin Oxide ( $\text{SnO}_x$ ) as Universal "Light-Soaking" Free Electron Extraction Material for Organic Solar Cells, Adv. Energy Mater. 5 (2015) 1500277.

[12] Z.M. Jarzebski, J.P. Marton, Physical Properties of  $\text{SnO}_2$  Materials II. Electrical Properties, J. Electrochem. Soc. 123 (1976) 299C.

[13] K.G. Godinho, A. Walsh, G.W. Watson, Energetic and Electronic Structure Analysis of Intrinsic Defects in  $\text{SnO}$ , J. Phys. Chem. C 113 (2009) 439.

[14] T. Isono, T. Fukuda, K. Nakagawa, R. Usui, R. Satoh, E. Morinaga, Y. Mihara, Highly

Conductive SnO<sub>2</sub> Thin Films for Flat-panel Displays, J. Soc. Inf. Disp. 15 (2007) 161.

[15] Y. Ogo, H. Hiramatsu, K. Nomura, H. Yanagi, T. Kamiya, M. Kimura, M. Hirano, H. Hosono, Tin Monoxide as an s-orbital-based p-type Oxide Semiconductor: Electronic Structures and TFT Application, Phys. Status Solidi A 206 (2009) 2187.

[16] A. Togo, F. Oba, I. Tanaka, K. Tatsumi, First-principles Calculations of Native Defects in Tin Monoxide, Phys. Rev. B 74 (2006) 195128.

[17] J.A. Caraveo-Frescas, P.K. Nayak, H.A. Al-Jawhari, D.B. Granato, U. Schwingenschlögl, H.N. Alshareef, Record Mobility in Transparent p-Type Tin Monoxide Films and Devices by Phase Engineering, ACS Nano 7 (2013) 5160.

[18] K. Okamura, B. Nasr, R.A. Brand, H. Hahn, Solution-processed Oxide Semiconductor SnO in p-channel Thin-film Transistors, J. Mater. Chem. 22 (2012) 4607.

[19] Y.-J. Choi, Y.-J. Han, C.-Y. Jeong, S.-H. Song, G.W. Baek, S.H. Jin, H.-I. Kwon, Enhancement Mode p-channel SnO Thin-film Transistors with Dual-gate Structures, J. Vac. Sci. Technol. B 33 (2015) 041203.

[20] F.C. Stedile, B.A. S. De Barros Jr., C.V. Barros Leite, F.L. Freire Jr., I.J.R. Baumvol, W.H. Schreiner, Characterization of Tin Oxide Thin Films Deposited by Reactive Sputtering, Thin Solid Film 170 (1989) 285.

[21] T. Brousse, D.M. Schleich, Sprayed and Thermally Evaporated SnO<sub>2</sub> Thin Films for Ethanol Sensors, Sensors and Actuators B 31 (1996) 77.

[22] T. Okuno, T. Oshima, S.-D. Lee, S. Fujita, Growth of SnO<sub>2</sub> Crystalline Thin Films by Mist Chemical Vapour Deposition Method, Phys. Status Solidi C 8 (2011) 540.

[23] H. Deng, F.J. Lamelas, J.M. Hossenlopp, Synthesis of Tin Oxide Nanocrystalline Phases via Use of Tin(II) Halide Precursors, Chem. Mater. 15 (2003) 2429.

- [24] H.-E. Cheng, D.-C. Tian, K.-C. Huang, Properties of SnO<sub>2</sub> Films Grown by Atomic Layer Deposition, *Procedia Engineering* 36 (2012) 510.
- [25] J. Sundqvist, A. Tarre, A. Rosental, A. Hårsta, Atomic Layer Deposition of Epitaxial and Polycrystalline SnO<sub>2</sub> Films from the SnI<sub>4</sub>/O<sub>2</sub> Precursor Combination, *Chem. Vap. Deposition* 9 (2003) 21.
- [26] D.-W. Choi, W.J. Maeng, J.-S. Park, The Conducting Tin Oxide Thin Films Deposited via Atomic Layer Deposition using Tetrakis-dimethylamino Tin and Peroxide for Transparent Flexible Electronics, *Appl. Surf. Sci.* 313 (2014) 585.
- [27] J.W. Elam, D.A. Baker, A.J. Hryn, A.B.F. Martinson, M.J. Pellin, J.T. Hupp, Atomic Layer Deposition of Tin Oxide Films using Tetrakis(dimethylamino)tin, *J. Vac. Sci. Technol. A* 26 (2008) 244.
- [28] M.N. Mullings, C. Hägglund, S.F. Bent, Tin Oxide Atomic Layer Deposition from Tetrakis(dimethylamino)tin and Water, *J. Vac. Sci. Technol. A* 31 (2013) 061503-1.
- [29] G. Choi, L. Satyanarayana, J. Park, Effect of Process Parameters on Surface Morphology and Characterization of PE-ALD SnO<sub>2</sub> Thin Films for Gas Sensing, *Appl. Surf. Sci.* 252 (2006) 7878.
- [30] V. Aravindan, K.B. Jinesh, R.R. Prabhakar, V.S. Kale, S. Madhavi, Atomic Layer Deposited (ALD) SnO<sub>2</sub> Anodes with Exceptional Cycleability for Li-ion Batteries, *Nano Energy* 2 (2013) 720.
- [31] L.Y. Liang, Z.M. Liu, H.T. Cao, X. Q. Pan, Microstructural, Optical, and Electrical Properties of SnO Thin Films Prepared on Quartz via a Two-Step Method, *ACS Appl. Mater. Interfaces* 2 (2010) 1060.

- [32] H. Giefers, F. Porsch, G. Wortmann, Kinetics of the Disproportionation of SnO, *Solid State Ionics* 176 (2005) 199.
- [33] J.H. Han, Y.J. Chung, B.K. Park, S.K. Kim, H.-S. Kim, C.G. Kim, T.-M. Chung, Growth of p-Type Tin(II) Monoxide Thin Films by Atomic Layer Deposition from Bis(1-dimethylamino-2-methyl-2propoxy)tin and H<sub>2</sub>O, *Chem. Mater.* 26 (2014) 6088.
- [34] S.H. Kim, I.-H. Baek, D.H. Kim, J.J. Pyeon, T.-M. Chung, S.-H. Baek, J.-S. Kim, J.H. Han, S.K. Kim, Fabrication of High-performance p-type Thin Film Transistors using Atomic-layer-deposited SnO Films, *J. Mater. Chem. C* 5 (2017) 3139.
- [35] S.M. George, J.H. Nam, G.Y. Lee, J.H. Han, B.K. Park, C.G. Kim, D.J. Jeon, T.-M. Chung, *N*-Alkoxy Carboxamide Stabilized Tin(II) and Germanium(II) Complexes for Thin-Film Applications, *Eur. J. Inorg. Chem.* 2016 (2016) 5539.
- [36] V.R. Rai, S. Agarwal, Surface Reaction Mechanisms during Plasma-Assisted Atomic Layer Deposition of Titanium Dioxide, *J. Phys. Chem. C* 113 (2009) 12962.
- [37] H. Luo, L.Y. Liang, H.T. Cao, Z.M. Liu, F. Zhuge, Structural, Chemical, Optical, and Electrical Evolution of SnO<sub>x</sub> Films Deposited by Reactive rf Magnetron Sputtering, *ACS Appl. Mater. Interfaces* 4 (2012) 5673.
- [38] H. Yabuta, N. Kaji, R. Hayashi, H. Kumomi, K. Nomura, T. Kamiya, M. Hirano, H. Hosono, Sputtering Formation of p-type SnO Thin-film Transistors on Glass toward Oxide Complimentary Circuits, *Appl. Phys. Lett.* 97 (2010) 072111.
- [39] S.F. Rus, T.Z. Ward, A. Herklotz, Strain-induced Optical Band Gap Variation of SnO<sub>2</sub> Films, *Thin Solid Films* 615 (2016) 103.
- [40] Y.-C. Ji, H.-X. Zhang, X.-H. Zhang, Z.-Q. Li, Structures, Optical Properties, and Electrical Transport Processes of SnO<sub>2</sub> Films with Oxygen Deficiencies, *Phys. Status Solidi B* 250 (2013)

2145.

[41] J. Niinistö, A. Rahtu, M. Putkonen, M. Ritala, M. Leskelä, L. Niinistö, In Situ Quadrupole Mass Spectrometry Study of Atomic-Layer Deposition of  $\text{ZrO}_2$  Using  $\text{Cp}_2\text{Zr}(\text{CH}_3)_2$  and Water, *Langmuir* 21 (2005) 7321.

[42] J.H. Han, L. Nyns, A. Delabie, A. Franquet, S.V. Elshocht, C. Adelman, Reaction Chemistry during the Atomic Layer Deposition of  $\text{Sc}_2\text{O}_3$  and  $\text{Gd}_2\text{O}_3$  from  $\text{Sc}(\text{MeCp})_3$ ,  $\text{Gd}(\text{PrCp})_3$ , and  $\text{H}_2\text{O}$ , *Chem. Mater.* 26 (2014) 1404.

#### Figure captions

Fig. 1 Variations of growth rate in (a)  $\text{Sn}(\text{edpa})_2/\text{O}_2$ -plasma and (b)  $\text{Sn}(\text{edpa})_2/\text{H}_2\text{O}$  ALD processes at growth temperature of 120 °C as a function of Sn-precursor and reactant pulse lengths. (c) Changes in growth rate in  $\text{Sn}(\text{edpa})_2/\text{O}_2$ -plasma and  $\text{Sn}(\text{edpa})_2/\text{H}_2\text{O}$  ALD processes at various stage temperatures of 70–300 °C. (d) Refractive index of  $\text{SnO}_x$  films deposited with  $\text{Sn}(\text{edpa})_2/\text{O}_2$ -plasma and  $\text{Sn}(\text{edpa})_2/\text{H}_2\text{O}$  at 70–300 °C.

Fig. 2 (a) Sn 3d XP spectra of  $\text{SnO}_x$  films deposited by  $\text{O}_2$ -plasma or  $\text{H}_2\text{O}$  at different temperatures. XPS depth profiles of  $\text{SnO}_x$  films grown at 120 °C with (b)  $\text{Sn}(\text{edpa})_2/\text{O}_2$ -plasma and (c)  $\text{Sn}(\text{edpa})_2/\text{H}_2\text{O}$  processes.

Fig. 3 GAXRD patterns for  $\text{SnO}_x$  films grown at various temperatures using (a)  $\text{Sn}(\text{edpa})_2/\text{O}_2$ -plasma and (b)  $\text{Sn}(\text{edpa})_2/\text{H}_2\text{O}$  (c) XRD pattern of  $\text{SnO}$  film after  $\text{N}_2$ -ambient annealing at 450 °C.

Fig. 4 AFM images of as-deposited  $\text{SnO}_2$  films at (a) 120 °C and (b) 220 °C. Topography of  $\text{SnO}$  films deposited at (c) 120 °C, (d) 180 °C, and (e) 250 °C. Surface morphology of  $\text{SnO}$  film after post-deposition annealing at 450 °C in  $\text{N}_2$  ambient.

Fig. 5 Tauc plots of (a)  $\text{SnO}_2$  and (b)  $\text{SnO}$  films grown at different deposition temperatures. (c) Comparison of transmittances of  $\text{SnO}_2$  and  $\text{SnO}$  films deposited at 120 °C.

Fig. 6 Carrier concentration, Hall mobility, and resistivity of  $\text{SnO}_2$  films grown at 120–300 °C

Fig. 7 (a) Bright field TEM image of  $\text{SnO}_2/\text{SnO}$  nanolaminate grown on TiN substrate, (b) XPS depth profiles of  $\text{SnO}_2/\text{SnO}$  nanolaminate, and (c) HRTEM image of nanolaminate film near the  $\text{SnO}_2/\text{SnO}$  interface. The inset shows the FFT patterns of the marked areas.

Fig. 8 (a) Variations of  $\text{CO}_2^+$  ( $m/z = 44$ ) signal intensity during an ALD cycle of  $\text{SnO}_2$  and  $\text{SnO}$  processes. The inset shows the variation in the  $\text{NO}^+$  ( $m/z = 30$ ) signal during the process. (b) Variation for  $^t\text{Bu}^+$  ( $m/z = 57$ ) intensity during an ALD cycle of  $\text{SnO}_2$  and  $\text{SnO}$  processes. The inset shows the variation of the complete  $\text{edpaH}^+$  ( $m/z = 145$ ) ligand signal.

Fig. 1

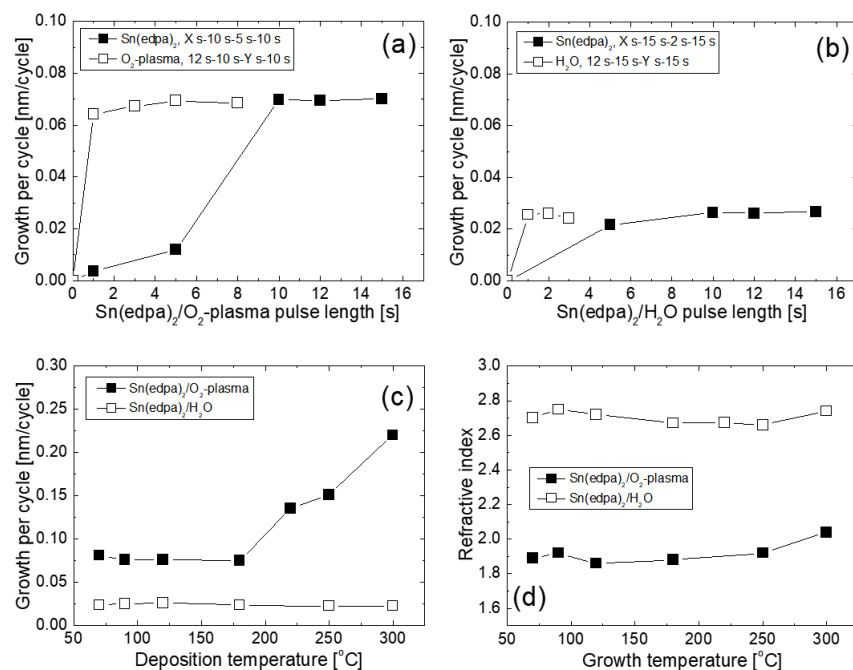


Fig. 2

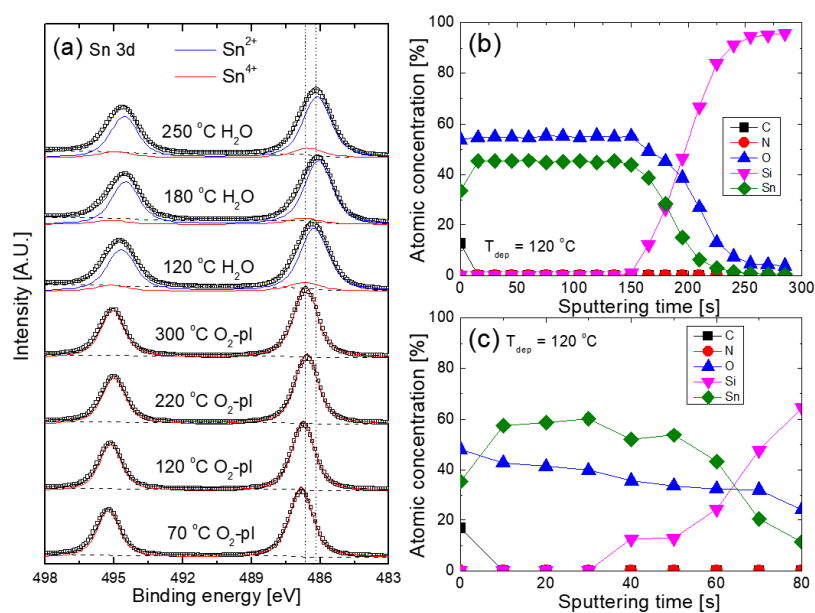




Fig. 3

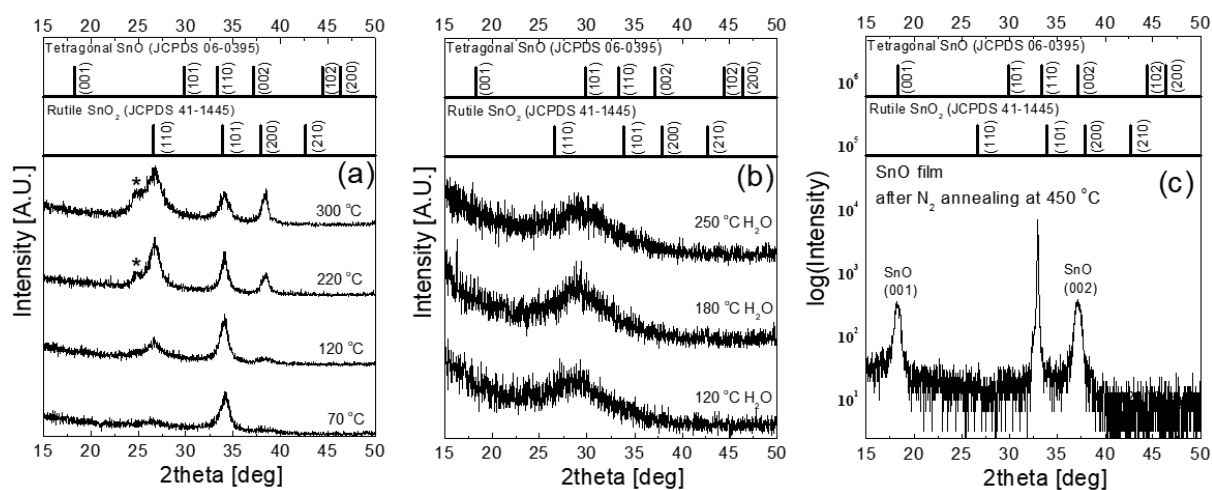


Fig. 4

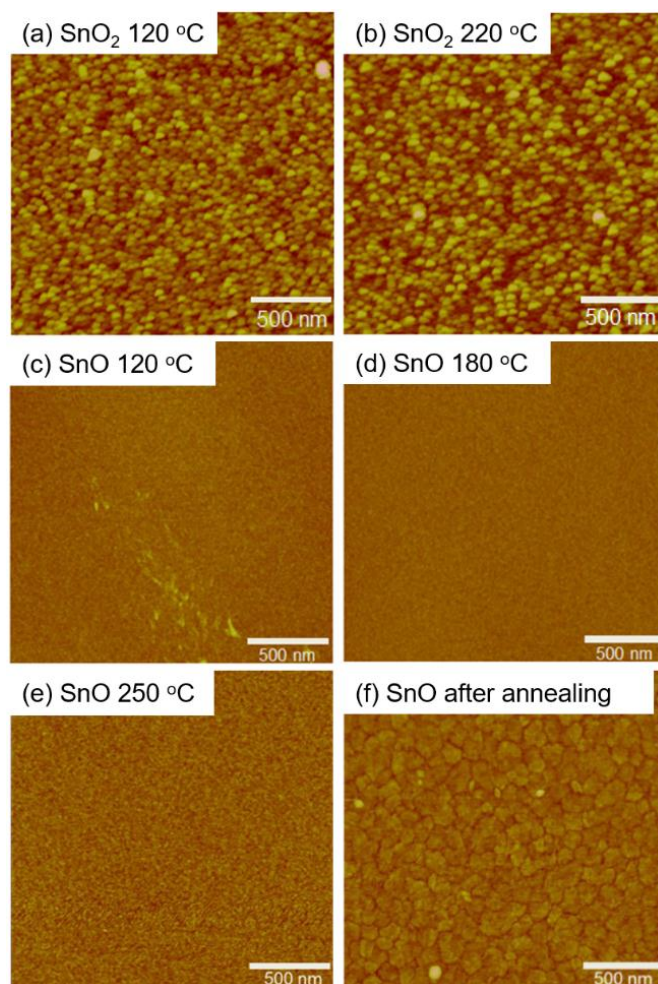


Fig. 5

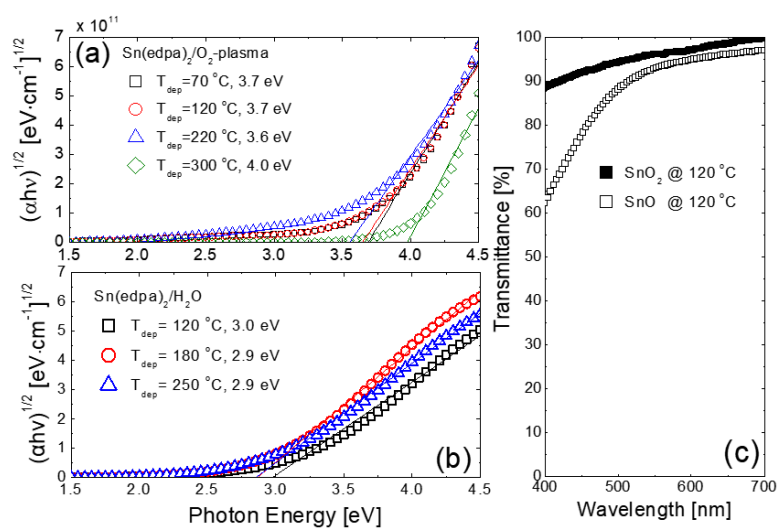


Fig. 6

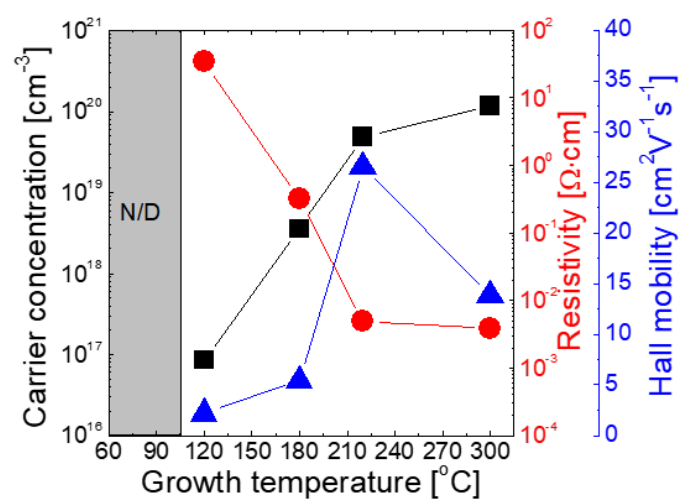


Fig. 7

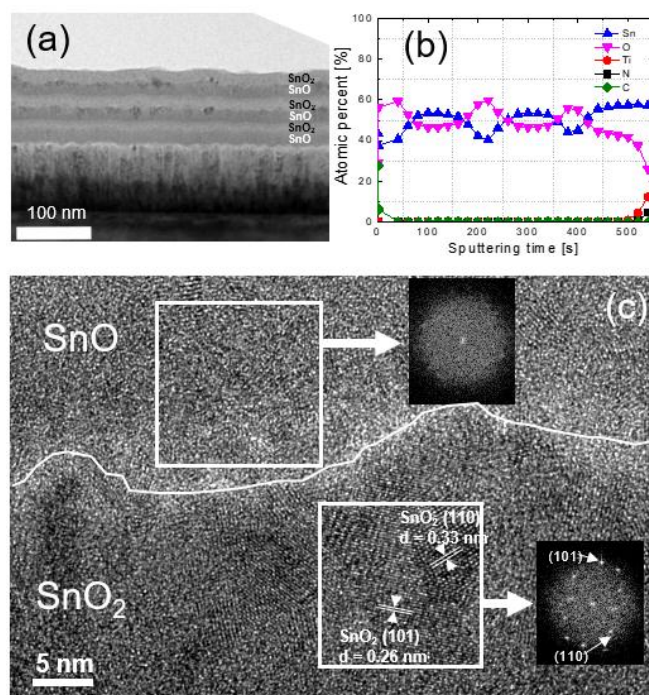


Fig. 8

